On the effect of copper as wetting agent during growth of thin silver films on silicon dioxide substrates

A. Jamnig, N. Pliatsikas, G. Abadias, K. Sarakinos

▶ **To cite this version:**

A. Jamnig, N. Pliatsikas, G. Abadias, K. Sarakinos. On the effect of copper as wetting agent during growth of thin silver films on silicon dioxide substrates. Applied Surface Science, 2021, 538, pp.148056. 10.1016/j.apsusc.2020.148056 . hal-03678344

HAL Id: hal-03678344
https://hal.science/hal-03678344

Submitted on 30 May 2022

HAL is a multi-disciplinary open access archive for the deposit and dissemination of scientific research documents, whether they are published or not. The documents may come from teaching and research institutions in France or abroad, or from public or private research centers.

L'archive ouverte pluridisciplinaire **HAL**, est destinée au dépôt et à la diffusion de documents scientifiques de niveau recherche, publiés ou non, émanant des établissements d'enseignement et de recherche français ou étrangers, des laboratoires publics ou privés.

Applied Surface Science 538 (2021) 148056

Contents lists available at ScienceDirect

Applied Surface Science

journal homepage: www.elsevier.com/locate/apsusc

On the effect of copper as wetting agent during growth of thin silver films on silicon dioxide substrates

A. Jamnig[a,b], N. Pliatsikas[a], G. Abadias[b], K. Sarakinos[a,*]

[a] Nanoscale Engineering Division, Department of Physics, Chemistry, and Biology, Linköping University, SE 581 83 Linköping, Sweden
[b] Institut Pprime, Département Physique et Mécanique des Matériaux, UPR 3346 CNRS, Université de Poitiers, 11 Bvd M. et P. Curie, TSA 41123, F86073 Poitiers Cedex 9, France

ARTICLE INFO

Keywords:
Silver
Thin films
Weakly-interacting substrates
Growth manipulation
In situ growth monitoring
Island coalescence

ABSTRACT

We study the effect of Cu incorporation on the morphological evolution and the optoelectronic properties of thin Ag films deposited by magnetron sputtering on weakly-interacting SiO_2 substrates. *In situ* and real time spectroscopic ellipsometry data show that by adding up to 4 at. % Cu throughout the entire film deposition process, wetting of the substrate by the metal layer is promoted, as evidenced by a decrease of the thickness at which the film becomes continuous from 19.5 nm (pure Ag) to 15 nm ($Ag_{96}Cu_4$). The *in situ* data are consistent with *ex situ* x-ray reflectometry analyses which show that Cu-containing films exhibit a root mean square roughness of 1.3 nm compared to the value 1.8 nm for pure Ag films, i.e., Cu leads to smoother film surfaces. These morphological changes are coupled with an increase in continuous-layer electrical resistivity from 1.0×10^{-5} Ωcm (Ag) to 1.25×10^{-5} Ωcm ($Ag_{96}Cu_4$). Scanning electron microscopic studies of discontinuous layers reveal that the presence of Cu at the film growth front promotes smooth surfaces (as compared to pure Ag films) by hindering the rate of island coalescence. To further understand the effect of Cu on film growth and electrical properties, in a second set of experiments, we deploy Cu with high temporal precision to target specific film-formation stages. The results show that longer presence of Cu in the vapor flux and the film growth front promote flat morphology. However, both a flat surface and a continuous-layer electrical resistivity that is equal to that of pure Ag films can only be achieved when Cu is deployed during the first 2.4 nm of film deposition, during which morphological evolution is, primarily, governed by island coalescence. Our overall results highlight potential pathways for fabricating high-quality multifunctional metal contacts in a wide range of optoelectronic devices based on weakly-interacting oxides and van der Waals materials.

1. Introduction

Thin (noble-) metal films deposited from the vapor phase on weakly-interacting oxides, semiconductors, and van der Waals materials exhibit a pronounced and uncontrolled three-dimensional (3D) morphology [1–3]. This is a major obstacle toward fabricating high-quality metal contacts and functional layers in a wide array of nanoelectronic [4–7], energy-saving, and energy-conversion devices [8–11]; which necessitates the development of methodologies for controllably influencing film growth and achieving two-dimensional (2D) morphology, so that the metal layer wets uniformly the underlying substrate.

Vapor-based thin film deposition is typically characterized by high supersaturation ratios at the vapor/solid interface, which yield a large driving force for condensation, and thereby, lead to far-from-equilibrium growth. As such, film morphological evolution is primarily governed by kinetic rates of atomic-scale mechanisms (e.g., adatom diffusion, corner-crossing, step edge-crossing) that affect the key initial formation stages of island nucleation, growth, and coalescence [12,13]. Variation of the most common deposition process parameters, including substrate temperature and deposition rate, has been routinely used to modify growth kinetics and the resulting film morphology [14]. This strategy is, however, not effective for selectively targeting film-formation stages and processes, so that growth can be manipulated in an efficient manner.

Selective manipulation of structure-forming processes to promote 2D growth morphology has been demonstrated for epitaxial metal-on-metal [15–19] and semiconductor-on-semiconductor systems [20,21], via deployment of minority metal and gaseous species (also referred to as surfactants) at the film surface. Concurrently, the atomistic mechanisms that control morphological evolution in weakly-interacting film/substrate systems are different than those in classical epitaxial

* Corresponding author.
E-mail address: kostas.sarakinos@liu.se (K. Sarakinos).

https://doi.org/10.1016/j.apsusc.2020.148056
Received 15 July 2020; Received in revised form 1 September 2020; Accepted 1 October 2020
Available online 06 October 2020
0169-4332/ © 2020 The Authors. Published by Elsevier B.V. This is an open access article under the CC BY license (http://creativecommons.org/licenses/by/4.0/).

growth theory [13,22,23], such that conventional surfactant-based strategies are not directly applicable for manipulating growth of noble-metal films on oxides and van der Waals materials. Despite the latter, there are studies in which less-noble metal (e.g., Nb, Ti, Cr) [5,24,25] and gaseous species (e.g., N_2, O_2) [9–11,26,27] have been shown to suppress the tendency of Ag and Cu films to grow in a 3D fashion on various oxide substrates. This, however, comes at cost of affecting other metal-layer physical properties (e.g., conductivity) [9,11,26,28]; which underscores the need to establish a fundamental understanding of the effect of surfactant (i.e., minority) species at various stages of thin noble-metal film growth on weakly-interacting substrates, in order to develop efficient and non-invasive morphology manipulation strategies.

We have recently contributed to the afore-mentioned understanding by sputter-depositing Ag films on SiO_2 substrates in mixed Ar-N_2 and Ar-O_2 gas atmospheres [28,29]. Our data showed that the presence of both N_2 and O_2 in the sputtering gas promotes 2D growth by decreasing the rates of island coalescence completion, while N_2 and O_2 are only incorporated in the film in trace amounts. Based on these insights, we demonstrated that morphology can be manipulated from 3D to 2D, without compromising the Ag layer electrical conductivity, if N_2 and O_2 are deployed with high temporal precision to selectively target the initial stages of island nucleation, growth, and coalescence.

In the present study, we explore the viability of the growth manipulation approach introduced in our recent works [28,29] using less-noble metals, instead of gaseous species, for promoting 2D morphology during deposition of Ag on SiO_2. We choose Cu as wetting agent, since it exhibits a less pronounced tendency for 3D growth than Ag [14], and it is relatively insensitive (i.e., inert) to interaction with impurities and the substrate material, compared to other metals (e.g., Al and group 4, 5, and 6 transition metals) that have been used in the literature for promoting 2D growth morphology [26,30]. Moreover, Cu is immiscible to Ag [31–33], which allows to selectively study its effect on surface growth kinetics without modifying the intrinsic bulk chemistry of the metal layer.

We monitor the evolution of the optoelectronic properties of percolated films *in situ* and in real time, and show that by increasing the Cu content in the metal layer up to 4 at. % the thickness at which the film becomes continuous decreases from 19.5 nm (pure Ag) to 15.0 nm ($Ag_{96}Cu_4$), while further increase of the Cu content up to 13 at. % does not have an appreciable effect on the value of the continuous film formation thickness. The *in situ* analysis is complemented by *ex situ* film characterization, which shows that Cu leads to flatter film morphologies—the film surface roughness decreases from 1.8 to 1.3 nm upon increasing Cu content from 0 to 4 at. %—i.e., 2D growth is promoted. Concurrently, the presence of Cu in the metal layer causes the film resistivity to increase monotonously from 1.0×10^{-5} Ωcm (pure Ag) to 1.25×10^{-5} Ωcm ($Ag_{96}Cu_4$) and 1.8×10^{-5} Ωcm ($Ag_{87}Cu_{13}$). Additional *ex situ* analyses of morphology of discontinuous films reveals that the decrease of the continuous-layer roughness with Cu addition has its origin in the initial film growth stages, whereby the presence of Cu delays reshaping of coalescing island clusters and promotes in-plane island growth.

To gain a better understanding of the effect of Cu on the overall film morphological evolution and electrical properties, we introduce Cu in the vapor flux during well-defined times. We find that the thickness of continuous film formation decreases with increasing time during which Cu is present in the deposition flux. However, by deploying Cu at the film growth front only during the first 20 s of deposition—corresponding to a nominal film thickness of 2.4 nm at which growth is primarily controlled by island coalescence—2D morphology can be promoted without compromising the metal-layer electrical conductivity. These findings, along with our previous results on the effect of N_2 [28] and O_2 [29] on Ag morphological evolution on SiO_2, pave the way toward a holistic platform for manipulating growth of noble-metal layers on weakly-interacting substrates in an efficient and non-invasive fashion.

2. Film growth and characterization

Thin films are synthesized by pulsed magnetron sputtering in an ultra-high vacuum (UHV) chamber (base pressure 10^{-8} Pa) on Si (1 0 0) substrates (thickness 525 μm), which are covered with 530 nm thermally grown SiO_2 layer. Experiments are performed using spatially separated magnetron sources equipped with elemental Ag and Cu targets (purity 99.99 at. %, diameter 76 mm, thickness 6 mm), which are placed 7.5 cm away from the substrate at an angle of 45° with respect to the substrate normal. Ar is used as working gas at a pressure of 1.3 Pa. Power with time-average density value of 0.2 W cm^{-2} is applied to the magnetrons in the form of unipolar square voltage pulses with a width of 50 μs and a frequency of 1 kHz, using MELEC SPIK 3000A pulsing units fed by ADL GS30 DC Power Supplies. A voltage pulse amplitude of $V_T^{Ag} = 485$ V is used for operating the Ag-equipped magnetron, while V_T^{Cu} is altered from 225 to 400 V, in order to vary the Ag-to-Cu vapor arrival ratio on the substrate and the Cu content in the film. Moreover, the V_T^{Ag} signal is used to trigger the pulsing unit supplying power to the Cu-equipped magnetron, such that the voltage pulses on both magnetrons are synchronous. No intentional heating is applied on the substrate during deposition, while the relatively small time-average target power density (0.2 W cm^{-2}) and the short deposition times (240 s) render an increase of the substrate temperature, due to plasma-surface interactions, highly unlikely.

To investigate the effect of Cu addition on different film growth stages, three deposition schemes are employed: (i) co-deposition of Ag and Cu throughout all film formation stages; (ii) co-deposition for a total time t_E during which the film growth front is exposed to Cu vapor flux, followed by deposition of pure Ag until growth completion; and (iii) initial deposition of pure Ag until power is applied to the Cu target after delay time t_D, so that growth is completed in the presence of both Ag and Cu vapor fluxes. Between each deposition run, the targets are sputter-cleaned for 10 min to eliminate cross-contamination of the magnetron sources.

Film growth is monitored *in situ* and in real time using a M-88 spectroscopic ellipsometer (J.A. Woollam Inc.). Ellipsometric angles Ψ and Δ are acquired at a rate of 0.5 s^{-1}, at an incidence angle of 70° with respect to the substrate normal, and incident-light photon energies between 1.6 and 3.2 eV. The optical response of the substrate is measured and modelled prior to film growth as Si substrate, covered with a SiO_2 layer with its thickness (530 nm) as fitting parameter. Reference data for Si and SiO_2 are taken from Herzinger et al. [34]

The optical response of percolated and continuous metal layers is described by the Drude free-electron model [35], according to which the complex dielectric function $\varepsilon_D(\omega)$ reads

$$\varepsilon_D(\omega) = \varepsilon_\infty - \frac{\omega_p^2}{\omega^2 + i\Gamma_D\omega}. \quad (1)$$

In Eq. (1), the parameter ε_∞ accounts for interband transitions occurring at higher values of ω than measured with the ellipsometer, Γ_D is the free-electron damping rate, and ω_p is the free-electron plasma frequency. From these fitting parameters, the electron scattering time $\tau = \hbar/\Gamma_D$ and the room-temperature resistivity $\rho = \Gamma_D/(\varepsilon_0\omega_p^2)$ can be calculated, where ε_0 is the vacuum permittivity. The above-described methodology has been shown in the literature [36–38] to provide an accurate description of optoelectronic properties of conducting films at various growth stages, and it is therefore used herein to study growth evolution of percolated and continuous Ag and Ag-Cu layers (see Sections 3.1 and 3.3)

An additional fitting parameter in the analysis of the ellipsometric data is the film height h_f, from which we extract the film deposition rate F by calculating the steady-state slope of h_f vs. deposition time t curves ($F = 0.120$ nm/s for Ag; $F = 0.120$ to 0.136 nm/s for Ag-Cu films in the V_T^{Cu} range 225 to 400 V). Based on F, we then calculate the nominal film thickness $\Theta = Ft$, which represents the number of deposited atoms at each stage of film growth.

Ellipsometric measurements are complemented by *ex situ* chemical, morphological, structural, and electrical analyses. Prior to removal from the deposition chamber, all samples that are used for *ex situ* characterization are capped with 3 nm thick layer of amorphous carbon (a–C), to avoid contamination and changes of the surface morphology upon atmospheric exposure. The capping layer is deposited by direct current magnetron sputtering from an elemental graphite target (purity 99.99 at. %, diameter 76 mm, thickness 6 mm), by applying a constant voltage of 460 V at an Ar working pressure of 1.3 Pa. The magnetron is placed 7.5 cm away from the substrate at an angle of 45° with respect to the substrate normal.

Sheet resistance of continuous Ag and Ag-Cu layers is measured *ex situ* at room temperature using a JANDEL four-point-probe setup (Model RM3000) with linear arrangement of the four probes. Film resistivity is then calculated by multiplying the sheet resistance value with the nominal film thickness, as obtained form *in situ* spectroscopic ellipsometry.

Film thickness, mass density, and a-C/metal-layer interface roughness in a-C/Ag-Cu/SiO_2/Si stacks are determined from x-ray reflectometry (XRR), performed in a Panalytical X'pert Pro diffractometer, equipped with a copper K_α source (wavelength 0.15418 nm) in line focus (operated with 45 kV and 40 mA), where a parallel beam mirror and a parallel-plate collimator are used in the incident and the reflected beam path, respectively. The reflected x-ray signal is processed with a X'Celerator/PIXcel-3D detector (Malvern Panalytical) operated in scanning line mode.

The crystal structure of Ag and Ag-Cu films is studied by X-ray diffractometry (XRD) in $\theta - 2\theta$ geometry, performed in the same instrument as the one used for XRR measurements. A nickel filter is used for removing copper K_β radiation. For crystallographic analysis, the texture coefficient $TC(h\ k\ l) = (I_{hkl}/I_{0,hkl})/\left(\frac{1}{N}\sum_N I_{hkl}/I_{0,hkl}\right)$ is calculated, where I_{hkl} is the experimentally recorded diffraction intensity of $(h\ k\ l)$ planes, $I_{0,hkl}$ are the corresponding $(h\ k\ l)$ intensities in reference Ag powder diffraction pattern [39], and N is the number of diffraction peaks used for calculating the texture coefficient.

Film morphology is studied by scanning electron microscopy (SEM) performed in a LEO 1550 Gemini microscope, with 5 kV acceleration voltage, and 3 mm working distance utilizing the InLens detector. The ImageJ software package[40] is used to quantify island number densities, size distribution, and shape, as well as substrate area coverage, by analyzing SEM images of a series of non-continuous films with Θ = 2.4, 3.6, and 6.0 nm.

The Ag-to-Cu ratio is determined by performing energy-dispersive X-ray spectroscopy (EDS) measurements on 200 nm thick AgCu films, in the same instrument as the SEM analysis, with 20 kV acceleration voltage and 8.5 mm working distance. Additional chemical composition analyses, including bonding configuration and spatial distribution of Cu in layers grown at various V_T^{Cu} values, are carried out by means of X-ray photoelectron spectroscopy (XPS) measurements on 25.0 nm thick Ag-Cu films. Photoelectron spectra are collected using a Kratos AXIS Ultra DLD UHV system (base pressure 4×10^{-8} Pa). Emission of photoelectrons is triggered by monochromated aluminum K_α X-rays, and their energies and intensities are measured using a hemispherical sector analyzer and a multichannel detector, in which core-level spectra are recorded with a 20 eV pass energy. Depth compositional profiles are acquired by etching the surface with a 4 keV Ar^+ ion beam, and ion-induced charging of the sample is corrected with respect to the Ar-*2p* peak, to account for shifts in the binding energy. Elemental analysis is performed with the Kratos Vision software and its sensitivity factor database.

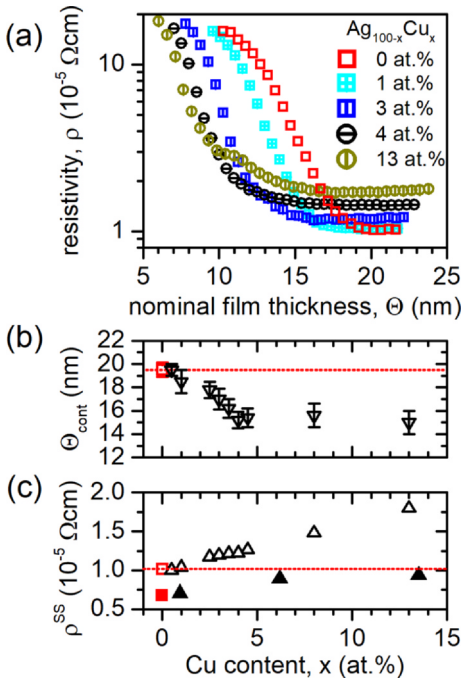

Fig. 1. (a) Resistivity (ρ) vs. nominal thickness (Θ) curves extracted from *in situ*, real-time spectroscopic ellipsometry measurements, of magnetron sputter-deposited Ag and $Ag_{100-x}Cu_x$ layers on SiO_2/Si substrates with increasing Cu content x in the film. Evolution of (b) the continuous film formation thickness Θ_{cont}, and (c) steady-state resistivity ρ^{SS} of $Ag_{100-x}Cu_x$ films vs. Cu content x in the film (hollow symbols). Room-temperature resistivity values of continuous $Ag_{100-x}Cu_x$ layers determined from *ex situ* four-point-probe measurements are also plotted in (c) (full symbols). Error bars correspond to the standard error from determining Θ_{cont} from resistivity vs. thickness plots presented in (a). The horizontal dotted lines represent the respective reference values for pure Ag films.

3. Results and discussion

3.1. Continuous film morphology, chemistry and microstructure

Fig. 1(a) presents the evolution of room-temperature resistivity ρ vs. nominal film thickness Θ for $Ag_{100-x}Cu_x$ films in the x range 0 to 13 at. %. For all ρ vs. Θ curves, ρ decreases initially by approximately an order of magnitude, after which decrease a steady-state resistivity ρ^{SS} is reached. The initial drop in resistivity indicates that the film is percolated (i.e., interconnected array of islands exists over the entire sample area), and the Θ value for which ρ^{SS} is reached corresponds to the continuous film formation thickness Θ_{cont}.[41] The data show that the increase of Cu content from 0 to 13 at. % results in a decrease of Θ_{cont} from 19.5 to 15.0 nm (i.e., a decrease by 23%). This indicates that Cu promotes wetting and 2D growth morphology. Concurrently, Cu incorporation leads to increase of resistivity from 1.0×10^{-5} to 1.8×10^{-5} Ωcm. This can be attributed to the larger room-temperature resistivity/shorter electron scattering time of bulk Cu (1.678 μΩcm/36.0 fs), compared to bulk Ag (1.587 μΩcm/36.8 fs) [42,43]. To better illustrate the effect of Cu on film morphology, we plot in Fig. 1(b) Θ_{cont} vs. x extracted from multiple sets of data similar to those in Fig. 1(a). Θ_{cont} decreases sharply from 19.5 to 15.0 nm in x range 0 to 4 at. % after which it saturates. The increase of steady-state resistivity with Cu addition is also seen by the data presented in Fig. 1(c) (hollow symbols). This trend is qualitatively confirmed by *ex situ* four-point-probe resistivity values plotted as full symbols in Fig. 1(c).

Based on the trends shown in Fig. 1(a) and (b), the remainder of the manuscript focuses on detailed comparison among Ag and $Ag_{96}Cu_4$ layers by employing *ex situ* techniques to study their morphology,

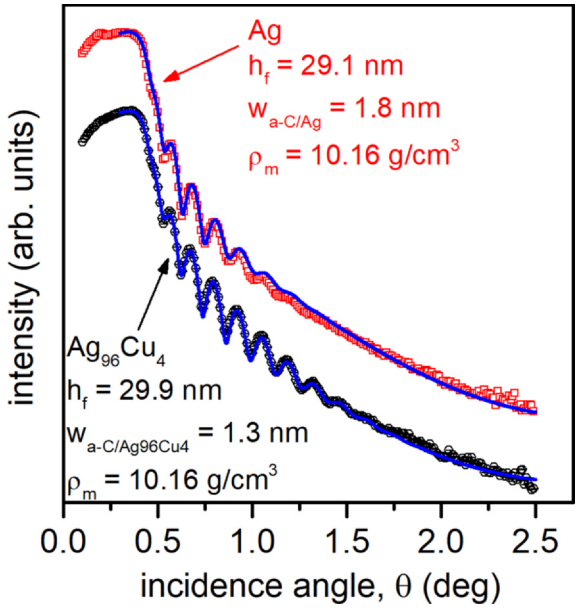

Fig. 2. X-ray reflectivity measurements of a-C/Ag/SiO_2/Si (red symbols) and a-C/$Ag_{96}Cu_4$/SiO_2/Si stacks (black symbols). The solid lines represent calculated reflectivity curves for fitting each data set, from which the metal-layer thickness h_f, mass density ρ_m, and a-C/Ag-Cu interface roughness ($w_{a-C/Ag}$ and $w_{a-C/Ag96Cu4}$) are determined. (For interpretation of the references to colour in this figure legend, the reader is referred to the web version of this article.)

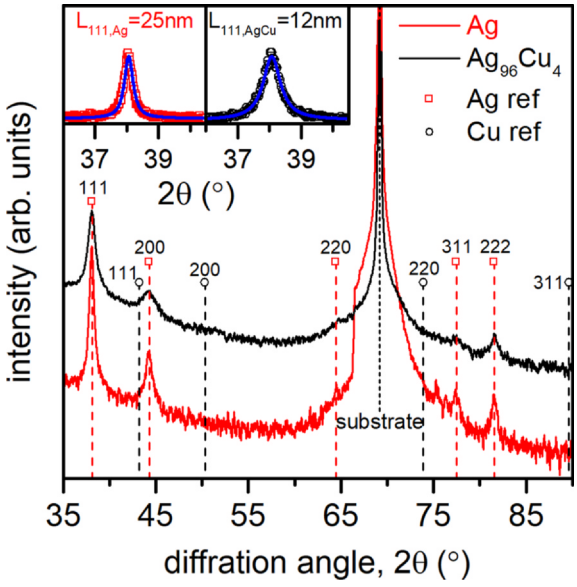

Fig. 3. X-ray diffractograms of 50 nm thick Ag and $Ag_{96}Cu_4$ films deposited on SiO_2/Si substrates. Peak positions of unstrained Ag [39], Cu [45] and Si [46] are indicated by vertical lines. The inserts show the (1 1 1) peak of Ag (left) and $Ag_{96}Cu_4$ (right) after baseline correction (symbols), and the Pseudo Voigt model fitted to the experimental data (lines). From the fit, the peak full width at half maximum, and thereby, the out-of-plane crystallite size L_{111} are determined.

microstructure, and bonding properties. Fig. 2 presents XRR data recorded from a-C/$Ag_{100-x}Cu_x$/SiO_2/Si stacks with $x = 0$ and 4 at. %, in which we have adjusted the metal-layer deposition time to obtain a nominal thickness of $\Theta = 30$ nm. Experimental data are represented by symbols, while calculated reflectivity curves, fitted to the measured data, are drawn as solid lines. From the fit we find that Ag and $Ag_{96}Cu_4$ layers have thicknesses (heights) $h_f = 29.1$ and 29.9 nm, respectively, which confirms the deposition rate established from spectroscopic ellipsometry. Furthermore, we see that both films have a mass density $\rho_m = 10.16$ g/cm^3, which is close to the bulk density of Ag (i.e., 10.49 g/cm^3) [44]. The latter is consistent with the *in situ* data in Fig. 1(a), showing that, for all Cu contents, the metal layers are continuous for >19 nm . Moreover, the Cu-containing film exhibits a smaller a-C/metal-layer interface root-mean-square roughness ($w_{a-C/Ag96Cu4} = 1.3$ nm) compared to the pure Ag film ($w_{a-C/Ag} = 1.8$ nm), which is consistent with the conclusion from Fig. 1(a) and (b) that addition of Cu promotes 2D growth morphology and flatter film surfaces.

X-ray diffractograms of 50 nm thick Ag and $Ag_{96}Cu_4$ films are presented in Fig. 3, where the positions of diffraction peaks of unstrained Ag [39], Cu [45] and Si(0 0 1) [46] are indicated by vertical lines in the graph. Both films have the face-centered cubic crystal structure of Ag, as evidenced by the presence of diffraction peaks corresponding to the (1 1 1), (2 0 0), (2 2 0), (3 1 1), and (2 2 2) crystallographic planes in the measured $\theta - 2\theta$ range. Texture analysis of the five observed diffraction peaks shows that $TC(111) = 2.1$ and 2.2 for Ag and AgCu films, respectively, indicating that both films exhibit a strong 111 crystallographic texture, which does not change by Cu addition. Moreover, no indication of formation of crystalline Cu domains that are detectable with XRD can be found in the $Ag_{96}Cu_4$ diffractogram.

The inserts in Fig. 3 show the (1 1 1) XRD lines of both films after base line correction (symbols), with solid lines corresponding to the best-fit of the experimental data using the Pseudo-Voigt function [47,48]. From the fit, we determine full-width at half-maximum (FWHM) values of 0. 33° and 0. 66° for Ag and $Ag_{96}Cu_4$, respectively. Applying Scherrer's equation [49], we calculate the out-of-plane size L_{111} of coherently diffracting domains in the film (i.e., crystallite size), which approximates the average grain size. Crystallites in the $Ag_{96}Cu_4$ film ($L_{111,AgCu} \cong 12$ nm) are smaller than in Ag ($L_{111,Ag} \cong 25$ nm); smaller grain sizes imply a larger grain boundary number density in the film, which favors charge-carrier scattering. Hence, the analysis presented in Fig. 3, in combination with the smaller bulk conductivity of Cu vs. Ag [42,43], is consistent with the larger resistivity in continuous $Ag_{96}Cu_4$ films compared to Ag (see Fig. 1(c)).

The results of XPS analyses, performed on an a-C/$Ag_{96}Cu_4$/SiO_2/Si stack (metal layer thickness 25 nm), are presented in Fig. 4. High-resolution core-level Ag-*3d* and Cu-*2p* scans recorded for the as-received stack and after etching of 2, 6, 14 and 24 nm of the stack surface are plotted in Fig. 4(a) and (b), respectively. Ag-*3d* data reveal the presence of the two doublets (*3/2* and *5/2*) at the expected positions (374.2 and 368.2 eV, respectively) [50] for Ag—Ag bonds. The peaks are symmetric, which means that no chemical interaction of Ag with Cu or other elements takes place. Cu-*2p* data in Fig. 4(b) show well defined Cu peaks (Cu-$2p_{1/2}$ at 952.5 eV and Cu-$2p_{3/2}$ at 933 eV) [51,52] corresponding to Cu—Cu bonds for all spectra. Concurrently the as-received scan shows clear peaks that correspond to Cu—O (933.6 eV) and Cu—OH (934.8 eV) [51]—as well as Cu—O satellite peaks—which can be attributed to contamination upon atmospheric exposure. Similarly, the scan after 24 nm etching shows a shoulder in the Cu-$2p_{3/2}$ peak that matches the position of Cu—O and Cu—OH bonds, which can be contributed to the interaction of Cu with the SiO_2 substrate.

Fig. 4(c) presents the evolution of the Cu atomic concentration x as function of the etching depth. Cu is detected throughout the film thickness, however, we find higher concentration of Cu close to the surface ($x = 16$ at. %) and toward the SiO_2 substrate ($x = 12$ at. %), as compared to intermediate etching depths (i.e., 2 nm to 14 nm), where $x \cong 5$ at. %. As Ag and Cu arrival rates are constant during the deposition process, the data in Fig. 4(c) indicate Cu segregation toward the SiO_2 substrate and the surface layer. Similar compositional profiles have been reported for the miscible Ag-Al system by Zhang et al. [30], who observed that Al segregates toward the film surface due to its tendency to form as aluminum-oxide. The latter may also explain the behavior of Cu which exhibits higher affinity toward oxygen as compared to Ag [53]. Another factor is the immiscibility of the Ag-Cu

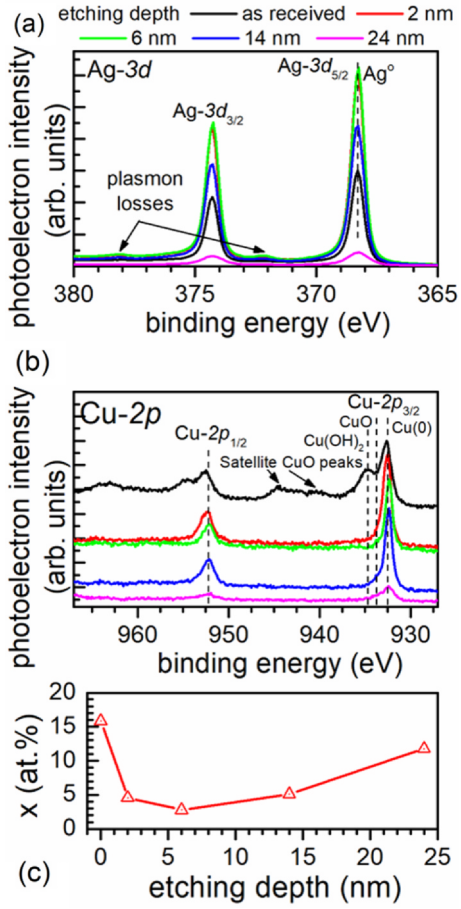

Fig. 4. (a) Ag-*3d* and (b) Cu-*2p* core level high resolution X-ray photoelectron spectra of a-C-capped 25 nm thick $Ag_{96}Cu_4$ thin films in the as-received state and after ion-beam etching of 2, 6, 14 and 24 nm. Ag plasmon loss peaks and positions for Cu-O binding states, as well as satellite peak positions are indicated. (c) Evolution of the atomic concentration x of Cu in the $Ag_{96}Cu_4$ film as function of ion-etching depth.

binary system which provides an additional driving force for phase separation [32,33].

3.2. Growth mechanisms and atomic-scale processes

To correlate the structural and morphological features of continuous metal layers established in Section 3.1 with initial film formation stages, we perform SEM analyses on a-C/$Ag_{100-x}Cu_x$/SiO_2/Si stacks (x = 0 and 4 at. %) in which the metal layers have nominal thicknesses Θ = 2.4, 3.6, and 6.0 nm. SEM images for pure Ag films (x = 0) are presented in Fig. 5(a)–(c). At Θ = 2.4 nm, the surface hosts isolated spherical islands/clusters, the size of which increases when increasing Θ to 3.6 and 6.0 nm. The size increase of islands/clusters with increasing Θ is accompanied by a gradual transition from spherical to more elongated shapes. This type of morphological evolution is typical in weakly-interacting film/substrate systems. Nanometer-size islands at the initial growth stages exhibit relatively short coalescence completion times (t_{coal}) so that, upon impingement, material is redistributed rapidly over the coalescing cluster and equilibrium shape (i.e., hemisphere) is re-established. With continued vapor deposition and coalescence completion events, the island size increases and eventually t_{coal} becomes longer than the time between successive island impingement events (t_{imp}). When the condition $t_{coal} > t_{imp}$ is fulfilled, coalescence is not completed (i.e., the island equilibrium shape is not retained), and the film surface is predominately populated by elongated clusters [13,14,41,54,55].

Addition of Cu does not change the overall morphological evolution (see Fig. 5(d)–(f)). However, islands are more elongated at Θ = 3.6 nm as compared to pure Ag films, while at Θ = 6.0 nm, the $Ag_{96}Cu_4$ film covers a larger fraction of the substrate, and is percolated. These findings indicate that Cu addition hinders material redistribution during coalescence (i.e., t_{coal} becomes longer), which promotes in-plane vs. out-of-plane island growth at the early stages of film formation, and ultimately, yields a decrease in continuous formation thickness and smaller surface roughness, as shown in Figs. 1 and 2. The slower material redistribution during coalescence may be attributed to solute drag, i.e., the decrease of grain boundary diffusivity due to the presence of Cu in the Ag lattice [56–58], resulting in incompletely coalesced islands with elongated shapes.

To quantify the trends observed in Fig. 5, we analyze SEM data to extract the evolution of the island size distribution for Ag and $Ag_{96}Cu_4$ films for nominal film thicknesses Θ = 2.4, 3.6, and 6.0 nm, and we determine mean island size (*MS*) and standard deviation (*SD*). For island shape analysis, islands are approximated by ellipses, and the aspect ratio (*AR*), i.e., the ratio of major to minor ellipse axis, is calculated. The results are presented in Fig. 6(a) through (c), whereby the data presented therein are obtained from images with smaller magnification than those presented in Fig. 5 for better statistics.

Fig. 6(a) displays data for both films with Θ = 2.4 nm and shows that the island size distributions are bell-shaped, with the distribution for the $Ag_{96}Cu_4$ film (black bars) shifted toward lower island sizes relative to that for the Ag film (red bars). This is also seen in the $MS \pm SD$ values which are 69 ± 46 nm^2 and 80 ± 51 nm^2 for $Ag_{96}Cu_4$ and Ag films, respectively. Concurrently, the mean in-plane *AR* of islands is 1.62 for $Ag_{96}Cu_4$, which is higher than the value 1.50 for Ag, indicating that islands are more elongated, and suggests that t_{coal} is increased due to the presence of Cu.

Increasing Θ to 3.6 nm shifts the overall island size distributions to larger values, as seen in Fig. 6(b) and reflected in the $MS \pm SD$ values for the $Ag_{96}Cu_4$ film (314 ± 248 nm^2) vs. that for Ag (234 ± 162 nm^2). Moreover, *AR* values increase compared toΘ = 2.4 nm, and remain larger for $Ag_{96}Cu_4$ (1.91) than for Ag (1.73), indicating more pronounced in-plane growth of islands.

At Θ = 6.0 nm, we find $MS \pm SD$ = 875 ± 881 nm^2 for Ag, with *AR* = 2.00 (see Fig. 6(c)). The comparatively large value of *SD* shows that island sizes do not follow normal distribution and is consistent with the formation of large structures on the surface seen in Fig. 5(c). For the $Ag_{96}Cu_4$ film, few very large islands are detected, that are highly interconnected, including one island with size 180000 nm^2 (not represented in Fig. 6(c)), which covers 40% of the observed substrate surface. This distribution is consistent with the percolated morphology of the $Ag_{96}Cu_4$ film at Θ = 6.0 nm in Fig. 5(f)). From the island size distributions in Fig. 6(a) through (c), we can establish that increasing *AR* values can be used as indication for incomplete coalescence, which leads to elongated island shapes, and percolated film structures. While, initially, island sizes for $Ag_{96}Cu_4$ are smaller than for Ag, the larger *AR* values indicate that addition of Cu expedites percolation and favors 2D growth morphology.

The SEM data are further quantified by calculating the substrate area coverage and the number density of islands/clusters as function of the nominal film thickness. The substrate coverage for Ag films (Fig. 6(d)) increases from 39 to 64%, when increasing Θ from 2.4 to 6.0 nm. For $Ag_{96}Cu_4$ films, this increase is more pronounced, and the coverage increases from 38 to 70% in the same thickness range. This trend confirms that deposition of Cu along with Ag vapor favors in-plane island growth and promotes 2D morphology.

The increase in coverage is accompanied by a decrease in the island/cluster number density, presented in Fig. 6(e), from 4.8×10^{15} to 7×10^{14} m^{-2} for Ag films. While the island/cluster number density is larger at Θ = 2.4 nm when Cu is present during the deposition (5.5×10^{15} m^{-2}), smaller values than that for Ag films are found for $\Theta \geq 3.6$ nm (e.g., 2×10^{14} m^{-2} for Θ = 6.0 nm). This may be

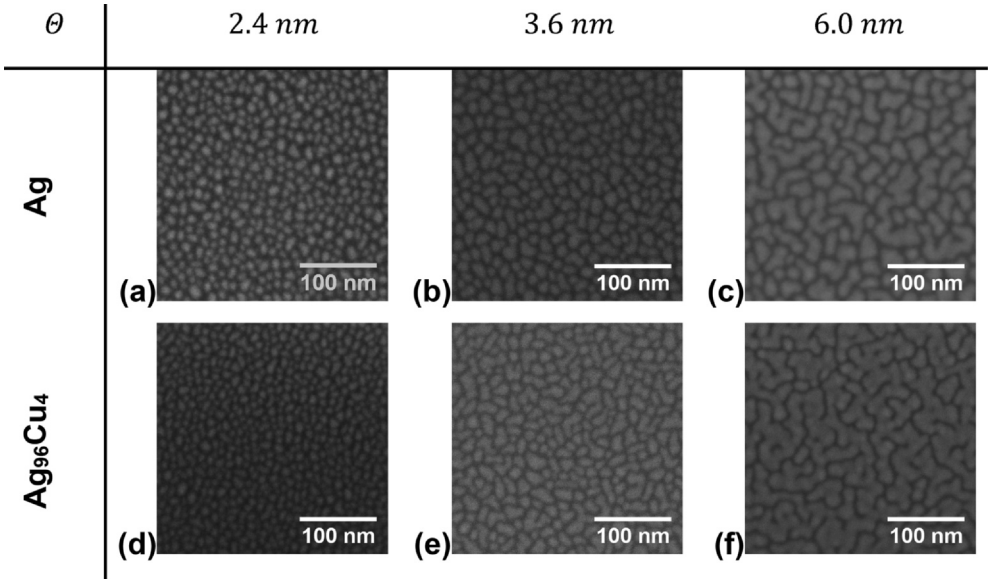

Fig. 5. Scanning electron microscopy images of Ag ((a), (b), (c)) and $Ag_{96}Cu_4$ films ((d), (e), (f)) with nominal thicknesses 2.4 nm ((a),(d)), 3.6 nm ((b), (e)), and 6.0 nm ((c), (f)).

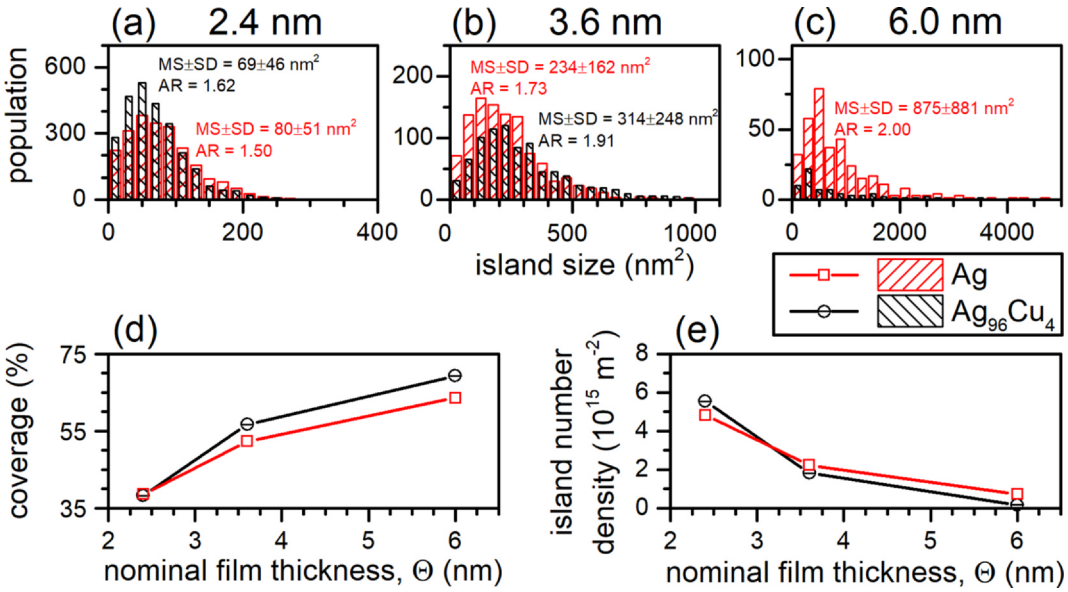

Fig. 6. (a)–(c) Island/cluster size distributions for discontinuous Ag and $Ag_{96}Cu_4$ films with nominal thicknesses of (a) 2.4 nm, (b) 3.6 nm and (c) 6.0 nm. Mean islands size (*MS*), standard deviation (*SD*), and mean aspect ratio (*AR*) of islands are given for films that consist mainly of isolated islands. In (c) island sizes >5000 nm^2 are not presented for Ag (one island with 10000 nm^2) and $Ag_{96}Cu_4$ films (eight islands ranging 7000 to 22000 nm^2, one island with 180000 nm^2). Evolution of (d) coverage and (e) island number density vs. nominal film thickness of Ag and $Ag_{96}Cu_4$ films. Data obtained by analyzing scanning electron micrographs with an area of 850 × 550 nm^2.

explained in light of previous studies which have suggested that Cu effectively decreases diffusion length of Ag on SiO_2, thereby increasing nucleation probability and island density.[59] However, simulations by Elofsson et al. [41] have estimated that saturation island density (i.e., the point at which island nucleation and growth rates are equal) occurs at $\Theta \cong 0.1$ nm for the case of perfectly hemispherical islands, i.e., the morphology established for $\Theta = 2.4$ nm in our SEM data is primarily governed by island coalescence. Hence, even though possible influence of Cu on surface diffusion and nucleation dynamics cannot be ruled out, we conclude that the morphological evolution in our films is primarily governed by the effect of Cu on island coalescence; which is consistent with recent studies on growth of Ag on SiO_2 and ZnO in nitrogen- and oxygen-containing gas atmospheres [26,28,29,60].

3.3. Selective copper deployment

We showed in Section 3.2 that Cu promotes 2D growth by increasing coalescence completion time, resulting in earlier onset of island interconnectivity. These morphological changes are accompanied by an increase in the electrical resistivity of continuous layers (see Section 3.1). Hence, two additional series of deposition experiments are conducted, aiming to study the effect of Cu on specific stages of the Ag film formation, and gauge the ability of Cu to change growth morphology, without compromising the film electrical properties, when released with high temporal precision: (i) in a first series, Cu is co-deposited with Ag for an exposure time t_E after which Cu supply is stopped and growth continues with Ag vapor until deposition is completed; (ii) in a second series, deposition starts with Ag vapor and Cu

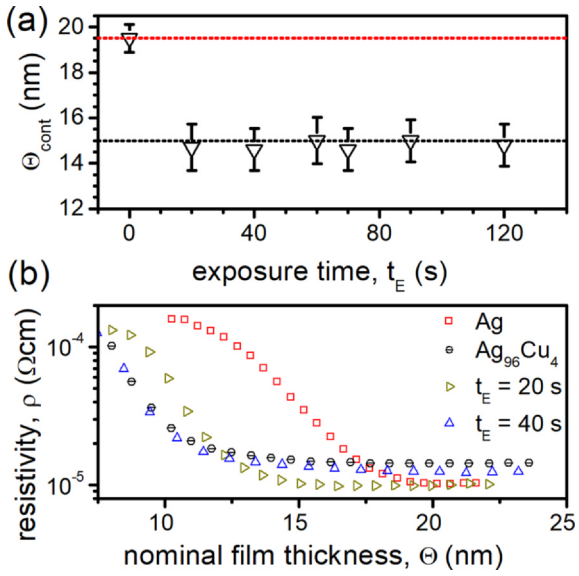

Fig. 7. (a) Evolution of the continuous film formation thickness Θ_{cont} of $Ag_{100-x}Cu_x$ films vs. exposure time t_E to Cu. Error bars correspond to the standard error from determining Θ_{cont} from resistivity ρ vs. nominal film thickness Θ plots. Horizontal dotted lines mark Θ_{cont} for Ag (red) and co-deposited $Ag_{96}Cu_4$ film (black). (b) Evolution of ρ vs. Θ for Ag, $Ag_{96}Cu_4$ co-deposition (also presented in Fig. 1) and $Ag_{100-x}Cu_x$ with exposure times $t_E = 20$ s and 40 s. (For interpretation of the references to colour in this figure legend, the reader is referred to the web version of this article.)

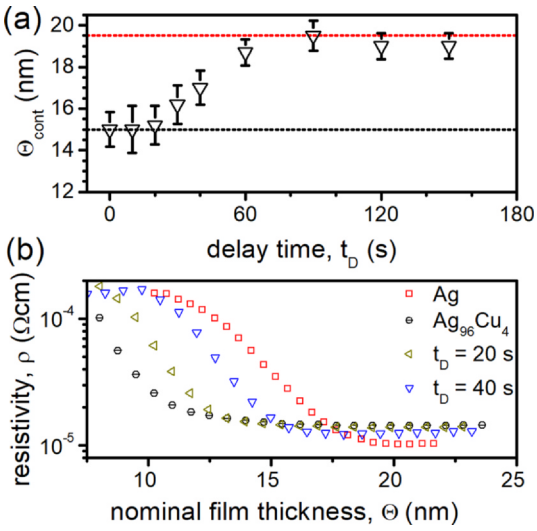

Fig. 8. (a) Evolution of the continuous film formation thickness Θ_{cont} of $Ag_{100-x}Cu_x$ films vs. delay time t_D of the Cu deposition. Error bars correspond to the standard error from determining Θ_{cont} from resistivity ρ vs. nominal thickness Θ plots. Horizontal dotted lines mark Θ_{cont} for Ag (red) and co-deposited $Ag_{96}Cu_4$ film (black). (b) Evolution of ρ vs. Θ for Ag, $Ag_{96}Cu_4$ co-deposition (also presented in Fig. 1) and $Ag_{100-x}Cu_x$ with delay times $t_D = 20$ s and 40 s. (For interpretation of the references to colour in this figure legend, the reader is referred to the web version of this article.)

vapor is added after a delay time $t_D$until deposition completion. We note that one set of deposition parameters is chosen for both experimental series, corresponding to the instantaneous Ag and Cu arrival rates for which $Ag_{96}Cu_4$ is grown. Hence, the global film composition changes depending on t_E and t_D.

Fig. 7(a) presents the evolution of Θ_{cont} with increasing values of t_E. The conditions $t_E = 0$ s and $t_E = 180$ s correspond to deposition of pure Ag and co-deposition of Ag and Cu yielding a $Ag_{96}Cu_4$ film, respectively, and are marked by horizontal dotted lines. For $t_E = 20$ s, $\Theta_{cont} = 14.7 \pm 1.0$ nm, which is very close to the value obtained for co-deposition (i.e., 15.0 nm) and lower than that of pure Ag (i.e., 19.5 nm). With increasing values of t_E, the Θ_{cont} value remains at 14.5 nm and does not evolve further. The evolution of the resistivity ρ vs nominal film thickness Θ for Ag, co-deposited $Ag_{96}Cu_4$ films and $Ag_{100-x}Cu_x$ films with $t_E = 20$ s and 40 s is presented in Fig. 7(b). From these curves, we find that the steady-state resistivity ρ^{SS} of the 20 s exposure sample is the same as in the pure Ag film, while it approaches the value of the co-deposited film when increasing t_E to 40 s. Exposure to Cu for 20 s can therefore decrease Θ_{cont}, while retaining the film resistivity from pure Ag films.

For the $t_E = 20$ s experiment, the mean Cu content in a 22.5 nm thick film is estimated to be $x = 0.4$ at. %. For comparable values of x in a co-deposited sample, the shift of Θ_{cont} can be expected to be minimal, e.g., we find $\Theta_{cont} = 18$ nm for $x = 1$ at. % in Fig. 1(b) compared to 19.5 nm for pure Ag. Thus, from ellipsometric data, we can conclude that addition of Cu during the first 20*s* of deposition (i.e., $\Theta \cong 2.4$ nm) is sufficient to hinder coalescence completion.

The evolution of Θ_{cont} with increasing values of t_D is presented in Fig. 8(a), where $t_D = 0$ s corresponds to co-deposition of Ag and Cu (Θ_{cont} is marked by black horizontal dotted line). For $t_D \leq 20$ s, Θ_{cont} remains at the value for co-deposition, i.e., 15.0 nm. Increasing t_D in the range 20 to 60 s leads to a monotonic increase in Θ_{cont}, and the value close to pure Ag deposition (i.e., 19.5 nm) is reached for $t_D \geq 60$ s. Fig. 8(b) presents ρ vs. Θ curves of Ag and $Ag_{96}Cu_4$ films as well as $Ag_{100-x}Cu_x$ films deposited with $t_D = 20$ s and 40 s. While a low value of $\Theta_{cont} \cong 15.2$ nm is reached for the shorter delay time, which is close to $Ag_{96}Cu_4$, ρ^{SS} is larger compared to pure Ag films. Increasing of t_D to 40 s leads to $\Theta_{cont} \cong 17.0$ nm, which is lower than pure Ag, but ρ^{SS}still remains larger compared to Ag.

In summary, the results from experiments in which Cu deposition is controlled via the exposure and delay times t_E and t_D, respectively, show that Θ_{cont} decreases (i.e., 2D growth morphology is promoted) with longer presence of Cu in the deposition flux and the film growth front, which is, e.g., facilitated by smaller t_D values. However, both smaller-than-pure-Ag Θ_{cont} values and ρ^{SS} that is identical to that of Ag films cannot be achieved, unless Cu is deployed during the initial growth stages to affect island coalescence.

4. Summary and outlook

The tendency of thin noble-metal films to grow in an uncontrolled three-dimensional fashion on weakly-interacting substrates, including oxides and van der Waals materials, can be reversed by deploying gaseous and/or less-noble metallic minority species at the film growth front. In this work, we investigate the effect Cu as wetting agent on the growth evolution of magnetron sputter-deposition of Ag films on SiO_2 substrates, which is an archetypal weakly-interacting film/substrate system. We show, by combining *in situ* and real-time spectroscopic ellipsometry with *ex situ* x-ray reflectometry, that the thickness at which a continuous film is formed can be decreased by 23% (i.e., from 19.5 to 15.0 nm) by steadily adding 4 at. % Cu to the Ag film, while the root-mean-square surface roughness decreases by 28% (from 1.8 to 1.3 nm). The addition of Cu is also accompanied by a 25% increase in film resistivity (from 1×10^{-5} to 1.25×10^{-5} Ωcm). Studies of the morphology of discontinuous layers using scanning electron microscopy reveal that Cu promotes two-dimensional growth and flat surface morphology by delaying island reshaping during coalescence. Moreover, we perform experiments in which Cu is deployed at the film growth front with high temporal precision to selectively target specific film-growth stages. By introducing Cu only during the first 20 s of deposition, so that island coalescence is targeted, we are able to promote 2D morphology without compromising the Ag-layer electrical conductivity. Our overall results expand the understanding with regards to the effect of minority species on film morphological evolution on weakly-interacting substrates and

provide the foundation for developing tailor-made strategies for non-invasive growth manipulation.

CRediT authorship contribution statement

A. Jamnig: Formal anaysis, Investigation, Writing - original draft. **N. Pliatsikas:** Formal analysis, Writing - review & editing. **G. Abadias:** Conceptualization, Methodology, Funding acquisition, Supervision, Writing - review & editing. **K. Sarakinos:** Conceptualization, Methodology, Funding acquisition, Supervision, Writing - review & editing.

Declaration of Competing Interest

The authors declare that they have no known competing financial interests or personal relationships that could have appeared to influence the work reported in this paper.

Acknowledgements

AJ and GA acknowledge the financial support of the French Government program “Investissements d’Avenir” (LABEX INTERACTIFS, reference ANR-11-LABX-0017-01). KS acknowledges financial support from Linköping University (“LiU Career Contract, Dnr-LiU-2015-01510, 2015-2020”) and the Swedish research council (contract VR-2015-04630). AJ and KS acknowledge financial support from the ÅForsk foundation (contracts ÅF 19-137 and ÅF 19-746). KS and NP acknowledge financial support from the Olle Engkvist foundation (contract SOEB 190-312) and the Wenner-Gren foundations (contracts UPD2018-0071 and UPD2019-0007).

References

[1] C.T. Campbell, Metal films and particles on oxide surfaces: structural, electronic and chemisorptive properties, J. Chem. Soc. Faraday Trans. 92 (1996) 1435, https://doi.org/10.1039/ft9969201435.
[2] X. Liu, Y. Han, J.W. Evans, A.K. Engstfeld, R.J. Behm, M.C. Tringides, M. Hupalo, H.-Q. Lin, L. Huang, K.-M. Ho, D. Appy, P.A. Thiel, C.-Z. Wang, Growth morphology and properties of metals on graphene, Prog. Surf. Sci. 90 (2015) 397–443, https://doi.org/10.1016/j.progsurf.2015.07.001.
[3] M.T. Hershberger, M. Hupalo, P.A. Thiel, C.Z. Wang, K.M. Ho, M.C. Tringides, Nonclassical “Explosive” nucleation in Pb/Si(111) at low temperatures, Phys. Rev. Lett. 113 (2014) 236101, , https://doi.org/10.1103/PhysRevLett.113.236101.
[4] C. Gong, C. Huang, J. Miller, L. Cheng, Y. Hao, D. Cobden, J. Kim, R.S. Ruoff, R.M. Wallace, K. Cho, X. Xu, Y.J. Chabal, Metal contacts on physical vapor deposited monolayer MoS2, ACS Nano 7 (2013) 11350–11357, https://doi.org/10.1021/nn4052138.
[5] J. Yun, Ultrathin metal films for transparent electrodes of flexible optoelectronic devices, Adv. Funct. Mater. 27 (2017) 1606641, https://doi.org/10.1002/adfm.201606641.
[6] I. Lee, J.-L. Lee, Transparent electrode of nanoscale metal film for optoelectronic devices, J. Photonics Energy 5 (2015) 057609, , https://doi.org/10.1117/1.JPE.5.057609.
[7] D. Gu, C. Zhang, Y.K. Wu, L.J. Guo, Ultrasmooth and thermally stable silver-based thin films with subnanometer roughness by aluminum doping, ACS Nano 8 (2014), https://doi.org/10.1021/nn503577c.
[8] K. Kato, H. Omoto, T. Tomioka, A. Takamatsu, Visible and near infrared light absorbance of Ag thin films deposited on ZnO under layers by magnetron sputtering, Sol. Energy Mater. Sol. Cells (2011), https://doi.org/10.1016/j.solmat.2011.04.005.
[9] G. Zhao, S.M. Kim, S.-G. Lee, T.-S. Bae, C. Mun, S. Lee, H. Yu, G.-H. Lee, H.-S. Lee, M. Song, J. Yun, Bendable solar cells from stable, flexible, and transparent conducting electrodes fabricated using a nitrogen-doped ultrathin copper film, Adv. Funct. Mater. 26 (2016) 4180–4191, https://doi.org/10.1002/adfm.201600392.
[10] G. Zhao, W. Shen, E. Jeong, S.-G. Lee, H.-S. Chung, T.-S. Bae, J.-S. Bae, G.-H. Lee, J. Tang, J. Yun, Nitrogen-mediated growth of silver nanocrystals to form ultrathin, high-purity silver-film electrodes with broad band transparency for solar cells, ACS Appl. Mater. Interfaces 10 (2018) 40901–40910, https://doi.org/10.1021/acsami.8b13377.
[11] W. Wang, M. Song, T.-S. Bae, Y.H. Park, Y.-C. Kang, S.-G. Lee, S.-Y. Kim, D.H. Kim, S. Lee, G. Min, G.-H. Lee, J.-W. Kang, J. Yun, Transparent ultrathin oxygen-doped silver electrodes for flexible organic solar cells, Adv. Funct. Mater. 24 (2014) 1551–1561, https://doi.org/10.1002/adfm.201301359.
[12] T. Michely, J. Krug, Islands, Mounds and Atoms, Springer Berlin Heidelberg, Berlin, Heidelberg, 2004. http://link.springer.com/10.1007/978-3-642-18672-1.
[13] V. Gervilla, G.A. Almyras, F. Thunström, J.E. Greene, K. Sarakinos, Dynamics of 3D-island growth on weakly-interacting substrates, Appl. Surf. Sci. 488 (2019) 383–390, https://doi.org/10.1016/j.apsusc.2019.05.208.
[14] A. Jamnig, D.G. Sangiovanni, G. Abadias, K. Sarakinos, Atomic-scale diffusion rates during growth of thin metal films on weakly-interacting substrates, Sci. Rep. 9 (2019) 6640, https://doi.org/10.1038/s41598-019-43107-8.
[15] H.A. van der Vegt, H.M. van Pinxteren, M. Lohmeier, E. Vlieg, J.M.C. Thornton, Surfactant-induced layer-by-layer growth of Ag on Ag(111), Phys. Rev. Lett. 68 (1992) 3335–3338, https://doi.org/10.1103/PhysRevLett.68.3335.
[16] H.A. van der Vegt, M. Breeman, S. Ferrer, V.H. Etgens, X. Torrelles, P. Fajardo, E. Vlieg, Indium-induced lowering of the Schwoebel barrier in the homoepitaxial growth of Cu(100), Phys. Rev. B. 51 (1995) 14806–14809, https://doi.org/10.1103/PhysRevB.51.14806.
[17] J. Vrijmoeth, H.A. van der Vegt, J.A. Meyer, E. Vlieg, R.J. Behm, Surfactant-induced layer-by-layer growth of Ag on Ag(111): origins and side effects, Phys. Rev. Lett. 72 (1994) 3843–3846, https://doi.org/10.1103/PhysRevLett.72.3843.
[18] S. Esch, M. Hohage, T. Michely, G. Comsa, Origin of oxygen induced layer-by-layer growth in homoepitaxy on Pt(111), Phys. Rev. Lett. 72 (1994) 518–521, https://doi.org/10.1103/PhysRevLett.72.518.
[19] B. Poelsema, R. Kunkel, N. Nagel, A.F. Becker, G. Rosenfeld, L.K. Verheij, G. Comsa, New phenomena in homoepitaxial growth of metals, Appl. Phys. A Solids Surfaces 53 (1991) 369–376, https://doi.org/10.1007/BF00348149.
[20] B. Voigtländer, A. Zinner, Influence of surfactants on the growth-kinetics of Si on Si (111), Surf. Sci. Lett. 292 (1993) L775–L780, https://doi.org/10.1016/0167-2584(93)90833-5.
[21] M. Horn-von Hoegen, J. Falta, M. Copel, R.M. Tromp, Surfactants in Si(111) homoepitaxy, Appl. Phys. Lett. 66 (1995) 487–489, https://doi.org/10.1063/1.114065.
[22] K. Sarakinos, A review on morphological evolution of thin metal films on weakly-interacting substrates, Thin Solid Films 688 (2019) 137312, , https://doi.org/10.1016/j.tsf.2019.05.031.
[23] B. Lü, G.A. Almyras, V. Gervilla, J.E. Greene, K. Sarakinos, Formation and morphological evolution of self-similar 3D nanostructures on weakly interacting substrates, Phys. Rev. Mater. 2 (2018) 063401, , https://doi.org/10.1103/PhysRevMaterials.2.063401.
[24] A. Anders, E. Byon, D.-H. Kim, K. Fukuda, S.H.N. Lim, Smoothing of ultrathin silver films by transition metal seeding, Solid State Commun. 140 (2006) 225–229, https://doi.org/10.1016/j.ssc.2006.08.027.
[25] K. Fukuda, S.H.N. Lim, A. Anders, Coalescence of magnetron-sputtered silver islands affected by transition metal seeding (Ni, Cr, Nb, Zr, Mo, W, Ta) and other parameters, Thin Solid Films 516 (2008) 4546–4552, https://doi.org/10.1016/j.tsf.2007.05.080.
[26] G. Zhao, E. Jeong, E.-A. Choi, S.M. Yu, J.-S. Bae, S.-G. Lee, S.Z. Han, G.-H. Lee, J. Yun, Strategy for improving Ag wetting on oxides: coalescence dynamics versus nucleation density, Appl. Surf. Sci. 510 (2020) 145515, , https://doi.org/10.1016/j.apsusc.2020.145515.
[27] J.M. Riveiro, P.S. Normile, J.P. Andrés, J.A. González, J.A. De Toro, T. Muñoz, P. Muñiz, Oxygen-assisted control of surface morphology in nonepitaxial sputter growth of Ag, Appl. Phys. Lett. 89 (2006) 201902, , https://doi.org/10.1063/1.2388140.
[28] A. Jamnig, N. Pliatsikas, M. Konpan, J. Lu, T. Kehagias, A.N. Kotanidis, N. Kalfagiannis, D.V. Bellas, E. Lidorikis, J. Kovac, G. Abadias, I. Petrov, J.E. Greene, K. Sarakinos, 3D-to-2D morphology manipulation of sputter-deposited nanoscale silver films on weakly interacting substrates via selective nitrogen deployment for multifunctional metal contacts, ACS Appl. Nano Mater. 3 (2020) 4728–4738, https://doi.org/10.1021/acsanm.0c00736.
[29] N. Pliatsikas, A. Jamnig, M. Konpan, A. Delimitis, G. Abadias, K. Sarakinos, Manipulation of thin silver film growth on weakly interacting silicon dioxide substrates using oxygen as a surfactant, J. Vac. Sci. Technol. A 38 (2020) 043406, , https://doi.org/10.1116/6.0000244.
[30] C. Zhang, N. Kinsey, L. Chen, C. Ji, M. Xu, M. Ferrera, X. Pan, V.M. Shalaev, A. Boltasseva, L.J. Guo, High-performance doped silver films: overcoming fundamental material limits for nanophotonic applications, Adv. Mater. 29 (2017) 1605177, https://doi.org/10.1002/adma.201605177.
[31] T. Kaub, R. Anthony, G.B. Thompson, Intrinsic stress response of low and high mobility solute additions to Cu thin films, J. Appl. Phys. 122 (2017) 225302, , https://doi.org/10.1063/1.5008269.
[32] V. Elofsson, G.A. Almyras, B. Lü, R.D. Boyd, K. Sarakinos, Atomic arrangement in immiscible Ag–Cu alloys synthesized far-from-equilibrium, Acta Mater. 110 (2016) 114–121, https://doi.org/10.1016/j.actamat.2016.03.023.
[33] V. Elofsson, G.A. Almyras, B. Lü, M. Garbrecht, R.D. Boyd, K. Sarakinos, Structure formation in Ag-X (XAu, Cu) alloys synthesized far-from-equilibrium, J. Appl. Phys. 123 (2018) 165301, , https://doi.org/10.1063/1.5018907.
[34] C.M. Herzinger, B. Johs, W.A. McGahan, J.A. Woollam, W. Paulson, Ellipsometric determination of optical constants for silicon and thermally grown silicon dioxide via a multi-sample, multi-wavelength, multi-angle investigation, J. Appl. Phys. 83 (1998) 3323–3336, https://doi.org/10.1063/1.367101.
[35] F. Wooten, Optical Properties of Solids, Academic Press, New York, 1972.
[36] P. Patsalas, S. Logothetidis, Optical, electronic, and transport properties of nanocrystalline titanium nitride thin films, J. Appl. Phys. 90 (2001) 4725–4734, https://doi.org/10.1063/1.1403677.
[37] T.W.H. Oates, A. Mücklich, Evolution of plasmon resonances during plasma deposition of silver nanoparticles, Nanotechnology 16 (2005) 2606–2611, https://doi.org/10.1088/0957-4484/16/11/023.
[38] L. Ryves, M.M.M. Bilek, T.W.H. Oates, R.N. Tarrant, D.R. McKenzie, F.A. Burgmann, D.G. McCulloch, Synthesis and in-situ ellipsometric monitoring of Ti/C

nanostructured multilayers using a high-current, dual source pulsed cathodic arc, Thin Solid Films 482 (2005) 133–137, https://doi.org/10.1016/j.tsf.2004.11.163.
[39] ICDD powder diffraction file no. 00-004-0787; silver, (n.d.).
[40] C.T. Rueden, J. Schindelin, M.C. Hiner, B.E. DeZonia, A.E. Walter, E.T. Arena, K.W. Eliceiri, Image J2: ImageJ for the next generation of scientific image data, BMC Bioinformatics 18 (2017) 529, https://doi.org/10.1186/s12859-017-1934-z.
[41] V. Elofsson, B. Lü, D. Magnfält, E.P. Münger, K. Sarakinos, Unravelling the physical mechanisms that determine microstructural evolution of ultrathin Volmer-Weber films, J. Appl. Phys. 116 (2014) 044302, , https://doi.org/10.1063/1.4890522.
[42] W.M. Haynes, CRC Handbook of chemistry and physics: a ready-reference book for chemical and physical data, ed. 58, CRC Press, Cleveland, Ohio, 1977.
[43] D. Gall, Electron mean free path in elemental metals, J. Appl. Phys. 119 (2016) 085101, , https://doi.org/10.1063/1.4942216.
[44] A.M. James, M.P. Lord, Macmillan's chemical and physical data, Macmillan, London, 1992. Doi: 10.1016/0307-4412(93)90067-A.
[45] ICDD powder diffraction file no. 01-070-3038; copper, (n.d.).
[46] ICDD powder diffraction file no. 00-027-1402; silicon, (n.d.).
[47] A. Hindeleh, D. Johnson, Crystallinity and crystallite size measurement in cellulose fibres: 1. Ramie and Fortisan, Polymer (Guildf) 13 (1972) 423–430, https://doi.org/10.1016/0032-3861(72)90107-3.
[48] T. de Keijser, E.J. Mittemeijer, H.C.F. Rozendaal, The determination of crystallite-size and lattice-strain parameters in conjunction with the profile-refinement method for the determination of crystal structures, J. Appl. Crystallogr. 16 (1983) 309–316, https://doi.org/10.1107/S0021889883010493.
[49] A.L. Patterson, The Scherrer formula for X-ray particle size determination, Phys. Rev. 56 (1939) 978–982, https://doi.org/10.1103/PhysRev.56.978.
[50] Y. Liu, R.G. Jordan, S.L. Qiu, Electronic structures of ordered Ag-Mg alloys, Phys. Rev. B. 49 (1994) 4478–4484, https://doi.org/10.1103/PhysRevB.49.4478.
[51] M.C. Biesinger, Advanced analysis of copper X-ray photoelectron spectra, Surf. Interface Anal. 49 (2017) 1325–1334, https://doi.org/10.1002/sia.6239.
[52] A.C. Miller, G.W. Simmons, Copper by XPS, Surf. Sci. Spectra 2 (1993) 55–60, https://doi.org/10.1116/1.1247725.
[53] A. Michaelides, V.A. Ranea, P.L. de Andres, D.A. King, General model for water monomer adsorption on close-packed transition and noble metal surfaces, Phys. Rev. Lett. 90 (2003) 216102, , https://doi.org/10.1103/PhysRevLett.90.216102.
[54] J. Carrey, J.-L. Maurice, Transition from droplet growth to percolation: Monte Carlo simulations and an analytical model, Phys. Rev. B. 63 (2001) 245408, , https://doi.org/10.1103/PhysRevB.63.245408.
[55] B. Lü, V. Elofsson, E.P. Münger, K. Sarakinos, Dynamic competition between island growth and coalescence in metal-on-insulator deposition, Appl. Phys. Lett. 105 (2014) 163107, , https://doi.org/10.1063/1.4900575.
[56] C.O. Jeong, N.S. Roh, S.G. Kim, H.S. Park, C.W. Kim, D.S. Sakong, J.H. Seok, K.H. Chung, W.H. Lee, D. Gan, P.S. Ho, B.S. Cho, B.J. Kang, H.J. Yang, Y.K. Ko, J.G. Lee, Feasibility of an Ag-alloy film as a thin-film transistor liquid-crystal display source/drain material, J. Electron. Mater. 31 (2002) 610–614, https://doi.org/10.1007/s11664-002-0132-5.
[57] F. Misják, P.B. Barna, G. Radnóczi, Growth of nanocomposite in eutectic Cu–Ag films, Thin Solid Films. 518 (2010) 4247–4251, https://doi.org/10.1016/j.tsf.2009.12.095.
[58] F.A. Nichols, Coalescence of two spheres by surface diffusion, J. Appl. Phys. 37 (1966) 2805–2808, https://doi.org/10.1063/1.1782127.
[59] H.-J. Kim, K.-W. Seo, H.-K. Kim, Y.-J. Noh, S.-I. Na, Ag-Pd-Cu alloy inserted transparent indium tin oxide electrodes for organic solar cells, J. Vac. Sci. Technol. A Vac. Surf. Film 32 (2014) 051507, , https://doi.org/10.1116/1.4891560.
[60] G. Zhao, W. Shen, E. Jeong, S.-G. Lee, S.M. Yu, T.-S. Bae, G.-H. Lee, S.Z. Han, J. Tang, E.-A. Choi, J. Yun, Ultrathin silver film electrodes with ultralow optical and electrical losses for flexible organic photovoltaics, ACS Appl. Mater. Interfaces 10 (2018) 27510–27520, https://doi.org/10.1021/acsami.8b08578.